Quantum Hall effect and Shubnikov–de Haas oscillations in a high-mobility *p*-type PbTe quantum well

F. S. Pena,[1] S. Wiedmann,[2] E. Abramof,[3] D. A. W. Soares,[1] P. H. O. Rappl,[3] S. de Castro,[4] and M. L. Peres[1]

[1]*Instituto de Física e Química, Universidade Federal de Itajubá, Itajubá, CEP 37500-903, Minas Gerais, Brazil*

[2]*High Field Magnet Laboratory (HFML-EMFL) & Institute for Molecules and Materials, Radboud University, 6525 ED, Nijmegen, The Netherlands*

[3]*Laboratório Associado de Sensores e Materiais, Instituto Nacional de Pesquisas Espaciais, São José dos Campos, CEP 12201-970, São Paulo, Brazil*

[4]*Universidade do Estado de Minas Gerais, Divinópolis – MG, CEP 35501-170, Minas Gerais, Brazil*

(Received 30 July 2020; revised 7 April 2021; accepted 10 May 2021; published 19 May 2021)

We present here the magnetotransport experiment performed with a magnetic field up to 30 T on a 10 nm-wide *p*-type PbTe quantum well. Pronounced Shubnikov–de Haas oscillations and the integer quantum Hall effect are clearly observed, demonstrating the transport of a confined two-dimensional hole gas with negligible parallel conduction at low temperatures. The sequence of filling factors can be explained by considering the magnetic field evolution of Landau levels derived from two longitudinal and one oblique occupied subbands and taking Zeeman spin splitting into account. During illumination, the total carrier density of the system is raised by 15%, which leads to a plateau sequence in the integer quantum Hall effect with higher filling factors in comparison to the dark condition.

DOI: 10.1103/PhysRevB.103.205305

I. INTRODUCTION

The optical and electrical properties of PbTe have been widely investigated over the years and have been applied in the development of infrared sensors [1,2], and laser diodes [3–5]. From the point of view of fundamental research, PbTe has very peculiar properties making this material system distinct from other semiconductors. For instance, its paraelectric character allows PbTe to present a huge static dielectric constant (∼1350 at 4.2 K) which can lead to a high charge carrier mobility (∼10^6 cm^2/V s). Likewise, it is possible to observe quantized conductance with considerable spin splitting of the plateaus already in magnetic fields about 0.2 T due to its high Landé *g* factor [6]. The strong spin-orbit coupling intrinsic to PbTe based compounds was experimentally investigated in symmetric [7] and antisymmetric quantum wells (QWs) [8]. In addition, PbTe was theoretically predicted to exhibit a dissipationless spin-Hall effect, without any accompanying charge current [9]. This makes PbTe compounds a promising candidate for the development of spintronic devices.

PbTe is part of the IV-VI family of the periodic table and its Fermi surface is composed of four equivalent ellipsoids with strong anisotropy ($K = m_{\parallel}/m_{\perp} \sim 10$), located at the *L* points of the Brillouin zone, where the longitudinal valley lies along the [111] direction and the three oblique valleys along the [$\bar{1}$11], [1$\bar{1}$1], [11$\bar{1}$] directions tilted 70.53° from the [111] axis. The multivalley character of the Fermi surface was investigated using high magnetic fields and low temperatures. Under these conditions, the integer quantum Hall effect (QHE) accompanied by Shubnikov–de Haas (SdH) in the longitudinal resistance oscillations are observed if the samples have high carrier mobility. From their analysis, it is possible to obtain information about the number of occupied electronic subbands and spin splitting in PbTe QW systems. For the *n*-type PbTe QW, a complete description of the electronic properties was presented in Ref. [10] and an anomalous sequence of filling factors was observed in the QHE due to multiple valleys. Recent photoconductivity measurements also revealed the contribution of multiple subbands in PbTe QWs giving rise to the anomalous behavior of photoconductivity amplitudes [11]. For *p*-type samples (in which holes are the majority carriers), neither quantitative nor qualitative results have been obtained so far. This is due to the difficulty of producing *p*-type samples with high crystalline quality and high electronic mobility.

In this work, we present magnetotransport measurements performed on a 10-nm-wide *p*-type PbTe QW grown by molecular beam epitaxy, which exhibits pronounced SdH oscillations and the integer QHE. Our results demonstrate the transport of a two-dimensional hole gas in a *p*-type PbTe quantum well with negligible parallel conduction at low temperatures. The confinement energies derived from the longitudinal and oblique valleys are calculated using a two-band $\boldsymbol{k}\cdot\boldsymbol{p}$ model within the envelope function approximation and the Fermi level is obtained by integrating over the two-dimensional density of states for all subbands to obtain iteratively the measured carrier density. We show that the filling factors sequence can be explained if one takes into account the magnetic field evolution of the occupied subband energies considering the individual Landau levels and Zeeman spin splitting. We also find that after illumination with a light-emitting diode (LED) the total carrier concentration of

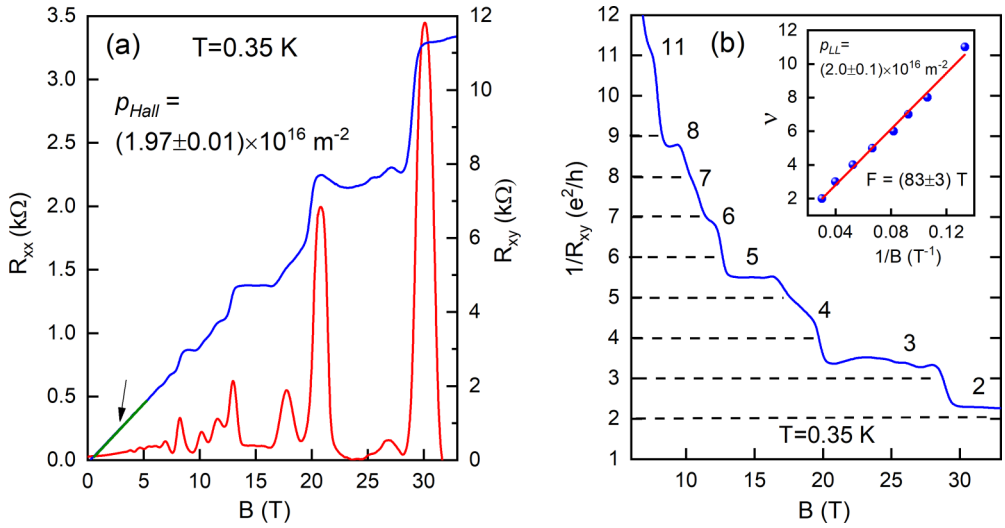

FIG. 1. (a) Longitudinal (R_{xx}) and transversal (R_{xy}) components of the electrical resistance as a function of the magnetic field applied perpendicularly to the *p*-type PbTe QW sample surface. The presence of the SdH oscillations and QHE in the curves of R_{xx} and R_{xy}, respectively, is clearly observed. The slope of R_{xy} at low magnetic fields represented by the green line (see arrow) gives the total Hall carrier density ($p_{\rm Hall}$). (b) The inverse of R_{xy} in units of (e^2/h) is plotted as a function of B. The assigned Landau level (LL) filling factors $\nu = 2, 3, 4, 5, 6, 7, 8$, and 11 are indicated on the plateaus. The dashed lines correspond to the exact values. The inset plots the filling factors as a function of the inverse magnetic field position of the R_{xx} minima. The linear fit (red line) gives the oscillations frequency F and the carrier density $p_{\rm LL}$ in the quantum well.

the system increases by 15% leading to a plateau sequence with higher filling factors in the integer QHE in comparison to the dark situation. Moreover, we perform temperature and angular dependencies of the longitudinal magnetoresistance that lead to further information on the PbTe multiple valley semiconductor system.

II. EXPERIMENT

The *p*-type PbTe single quantum well structure was grown by molecular beam epitaxy (MBE), using a Riber 32P system, on (111) BaF_2 monocrystal substrates with a cross section area of $15\times15\,\text{mm}^2$. In the beginning, during the preparation process, freshly cleaved thin slices of BaF_2 less than 1 mm thick were separated from the crystalline bar. Inside the MBE growth chamber, after the thermal cleaning process, the epitaxial structure deposition was carried out at a substrate temperature of 240 °C and the sample structure follows the sequence BaF_2/$Pb_{0.9}Eu_{0.1}Te$/PbTe/$Pb_{0.9}Eu_{0.1}Te$. First, a 2 μm $Pb_{0.9}Eu_{0.1}Te$ thick buffer layer (first barrier layer) was deposited on top of the (111) BaF_2 substrate, at a constant growth rate of 1.6 Å/sec; subsequently the 10 nm-thick PbTe single quantum well was grown, at a 1.3 Å/sec rate, and finally, the second $Pb_{0.9}Eu_{0.1}Te$ barrier layer of similar thickness and identical to the buffer growth conditions was deposited. The PbTe source is filled with nonstoichiometric charge, but intentionally metal rich, so that an additional tellurium flux was simultaneously sublimated to obtain an intrinsic *p*-type PbTe well. For the barriers, PbTe, Eu, and Te sources were used. The parallel conduction through the barriers is minimized by choosing an Eu content of $x = 0.1$ in the $Pb_{1-x}Eu_xTe$ barrier layers. At low temperatures (~10 K), the $Pb_{0.9}Eu_{0.1}$ Te barrier resistivity is 10^7 times higher than the one of the PbTe well. van der Pauw geometry samples were prepared by soldering 25 μm-thick gold wires with small indium pellets. Magnetotransport measurements were carried out at temperatures from 0.35 to 70 K in a ^{3}He system in a 33 T resistive (Bitter-type) magnet. We used the standard four-probe AC lock-in technique with a constant excitation current of 1.0 μA. After the first series of experiments, the measurements were taken with the sample illuminated with a red LED (wavelength 643 nm, diameter of 3 mm, and a current of 1 mA).

III. RESULTS AND DISCUSSION

A. Quantum Hall effect

Figure 1(a) presents the longitudinal (R_{xx}) and transversal (R_{xy}) components of the electrical resistance as a function of the magnetic field B applied perpendicularly to the PbTe QW sample surface at $T = 0.35$ K. Pronounced SdH oscillations and the integer QHE are clearly observed in the R_{xx} and R_{xy} traces, respectively. At 15 T, a wide plateau in R_{xy} and a nearly zero resistance in R_{xx} are found, demonstrating the high sample quality and the presence of a two-dimensional (2D) hole gas in the QW. At higher fields, the longitudinal resistance R_{xx} vanishes at the B intervals relative to the plateaus in R_{xy}. From the slope of R_{xy} at low magnetic fields, represented by the green line (see arrow) in Fig. 1(a), a total hole carrier density $p_{\rm Hall} = (1.97 \pm 0.01)\times10^{16}\,\text{m}^{-2}$ is extracted. Considering this hole concentration and the zero-field resistivity at $T = 0.35$ K, we obtain a hole mobility of $1.2\times10^5\,\text{cm}^2/\text{V s}$. This value is equivalent to the mobility found for the *n*-type PbTe QW sample [10], which also proves the quality of the *p*-type PbTe QW investigated here.

Figure 1(b) presents a plot of $1/R_{xy}$ in units of (e^2/h) as a function of B (blue curve), where h is the Planck constant and e is the electron charge. This plot would directly give the

values of the filling factors (see dashed lines). As the plateaus are not exactly at integer multiples of (e^2/h), we derive the correct sequence of filling factors related to the Landau level occupation using the expression $\nu = (hp_{\rm Hall}/eB)$, where the values of B are taken from the minima in R_{xx}, i.e., $B = 33$, 25, 19, 15, 12.2, 10.8, 9.4, and 7.5 T. These B values give the corresponding integer filling factors $\nu = 2$, 3, 4, 5, 6, 7, 8, and 11, which are assigned to the plateaus in Fig. 1(b). Even though the plateau related to the filling factor 7 is not defined, it is present as a minimum at 10.8 T in the R_{xx} curve. Next, we plot in the inset of Fig. 1(b) the Landau level filling factors ν as a function of inverse magnetic fields $(1/B)$ at which the R_{xx} minima occur. The expected linear behavior is observed and from the linear fit, we obtain the frequency of the oscillations F according to the relation $\nu \propto F/B$. The obtained value is $F = (83 \pm 3)$ T corresponding to a hole concentration $p_{\rm LL} = (2.0 \pm 0.1)\times 10^{16}$ m^{-2} in the quantum well. For this calculation, we used the relations $p = k_F^2/4\pi$ and $k_F^2 = 2Fe/\hbar$, where k_F is the Fermi wave vector and $\hbar$ is the reduced Planck constant. This value of $p_{\rm LL}$ is equal to the total Hall carrier density ($p_{\rm Hall}$) within the experimental error, indicating that the parallel conduction through the barriers is negligible at low temperatures. This result demonstrates the 2D transport of a hole gas in a p-type PbTe quantum well with no sign of parallel conduction.

B. Calculation of confinement and Fermi energies

The sequence of filling factors can be further investigated if one considers the magnetic field evolution of Landau levels including the Zeeman spin splitting of the subbands. For this purpose, it is necessary to know the confinement energies in the quantum well. To calculate the subband energies derived from the longitudinal and oblique valleys of our p-type PbTe well, we use the analytical model proposed in Ref. [12] based on the Dimmock two-band $\boldsymbol{k}\cdot\boldsymbol{p}$ theory [13] within the envelope function approximation. This model was applied to determine the optical transition energies in PbEuTe/PbTe multiple QWs [14] and the confinement levels for electrons in n-type $Pb_{0.9}Eu_{0.1}Te$/PbTe single QWs [10].

The confinement energies related to the longitudinal and oblique valleys for the p-type PbTe QW are solutions of the transcendental equations,

$$\frac{\chi}{m^B_{L,O}} = -\frac{q}{m^W_{L,O}}\tan\left(\frac{qL}{2}\right), \tag{1}$$

$$\frac{\chi}{m^B_{L,O}} = \frac{q}{m^W_{L,O}}\cot\left(\frac{qL}{2}\right), \tag{2}$$

which are obtained from the matching of the plane wave solutions of the well (W) and the barriers (B) at the interface, using the Ben-Daniel-Duke like boundary conditions. Equations (1) and (2) are relative to even and odd solutions, respectively, where L is the width of the quantum well ($L = 10$ nm in our case), and

$$\chi = -\sqrt{\left(2\, m^B_{L,O}/\hbar^2\right)(\Delta E_v - E)}, \tag{3}$$

$$q = \sqrt{\left(2\, m^W_{L,O}/\hbar^2\right)E} \tag{4}$$

TABLE I. Band structure parameters for the PbTe well and $Pb_{0.9}Eu_{0.1}Te$ barrier at 0.35 K: energy gap (Eg) and band-edge effective masses in units of the free electron mass (m_e).

Layer	Eg (eV)	$m_\parallel$	$m_\perp$	m_L	m_O	$m_L^{\rm cyc}$	$m_O^{\rm cyc}$
PbTe (W)	0.190	0.213	0.021	0.213	0.023	0.021	0.063
$Pb_{0.9}Eu_{0.1}Te$ (B)	0.638	0.536	0.066	0.536	0.073		

are the wave vectors of the barrier and the well, respectively, with the barrier height in the valence band given by ΔE_v.

From geometrical arguments, the confinement effective masses along the [111] direction for the longitudinal (m_L) and oblique (m_O) valleys are given in terms of the parallel ($m_\parallel$) and perpendicular ($m_\perp$) effective masses by $m_L = m_\parallel$ and $m_O = 9m_\parallel m_\perp/(8m_\parallel + m_\perp)$. Table I summarizes the band-edge effective mass values and energy gaps used here. Within the two-band $\boldsymbol{k}\cdot\boldsymbol{p}$ Dimmock model [12], the energy dependence of the effective mass is expressed by $m_{\parallel,\perp}(E) = (\frac{m_e}{2P^2_{\parallel,\perp}/m_e})(E + E_g)$, where $P_{\parallel,\perp}$ is the parallel (perpendicular) momentum interband matrix element. The effective matrix elements chosen here are those that reproduce the experimentally determined band-edge effective masses $m_{\parallel,\perp}(0)$ listed in Table I, i.e., $2P^2_{\parallel,\perp}/m_e = [m_e/m_{\parallel,\perp}(0)]E_g$. Using this approach, the energy-dependent effective mass for the PbTe well becomes $m^W_{\parallel,\perp}(E) = m^W_{\parallel,\perp}(0) + m^W_{\parallel,\perp}(0)\ [E/E_g^W]$. Assuming that the momentum interband matrix elements of the PbEuTe barriers are the same as for the well, the relation $m^B_{\parallel,\perp}(E) = m^B_{\parallel,\perp}(0) + m^W_{\parallel,\perp}(0)\ [E/E_g^B]$ gives the barriers effective mass as a function of energy. Also, the cyclotronic mass obtained from the projection of the mass ellipsoid on the $k_x - k_y$ plane is given for each valley by $m_L^{\rm cyc} = m_\perp$ and $m_O^{\rm cyc} = \frac{1}{3}m_\perp\sqrt{(1 + 8\frac{m_\parallel}{m_\perp})}$. The values of the cyclotronic masses are also displayed in Table I.

Using the energy gap values at a temperature of 0.35 K given in Table I for the PbTe well and $Pb_{0.9}Eu_{0.1}Te$ barriers and considering a 55:45 conduction to valence-band offset ($Q = 0.55$) [10], the barrier height for the holes is $\Delta E_v = (1-Q)\ \Delta E_g = 0.202$ eV. Figure 2(a) shows the numerical solution of the transcendental equations (1) and (2) in the negative part of the coordinate axis (valence band) for longitudinal (blue lines) and oblique (red lines) valleys of our 10 nm-wide p-type PbTe quantum well. The confinement energy values are obtained from the intersection points indicated by arrows. The subband energies, relative to the valence band edge, are 10, 38, 77, 121, and 168 meV for the longitudinal valley, and 42 and 149 meV for the oblique valleys in the p-type PbTe QW. These subbands are represented in the energy diagram shown in Fig. 2(b).

We can calculate the Fermi level by integrating over the two-dimensional density of states for all subbands to obtain iteratively the measured carrier density. In this calculation at low temperatures ($T = 0.35$ K), the 2D density of states is a step function that increases by $1\times\pi\hbar^2/m_L^{\rm cyc}$ or by $3\times\pi\hbar^2/m_O^{\rm cyc}$ each time the energy crosses a longitudinal or an oblique level, respectively. The values of 1 and 3 correspond to the valley degeneracy. Using the 2D carrier concentration at 0.35 K from the inset in Fig. 1(b) and the values of the

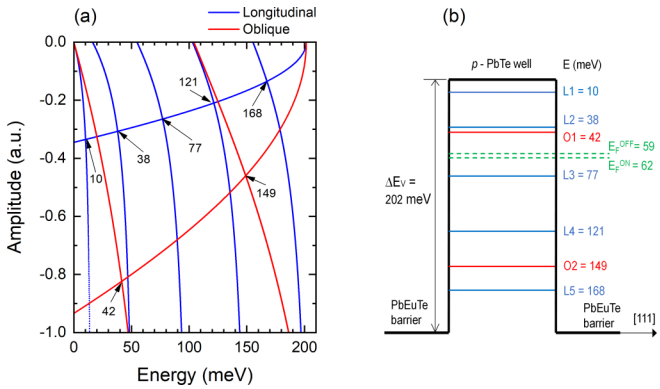

FIG. 2. (a) Confinement energies at low temperatures for the longitudinal (blue lines) and oblique (red lines) valleys of the 10-nm-wide *p*-type PbTe quantum well obtained from the intersection points, indicated by arrows, of the transcendental equations (1) and (2) in the negative part of the coordinate axis (valence band). (b) Energy diagram of the PbTe QW indicating the position of the longitudinal (L) and oblique (O) confinement energies together with the Fermi energies (dashed green lines) under dark and illuminated conditions.

cyclotronic masses m_L^{cyc} and m_O^{cyc} given in Table I, we obtain the value of $E_F = (59 \pm 1)$ meV for our *p*-type PbTe QW at dark conditions. This Fermi energy position is also marked in the energy diagram of Fig. 2(b), showing that the first and second longitudinal and the first oblique subbands are occupied.

C. Evolution of Landau levels and Zeeman spin splitting

The magnetic field evolution of Landau levels (LLs) and Zeeman spin splitting for the subbands can be computed using the Mitchell and Wallis formalism [15–17] also applied to the *n*-type PbTe QW in Ref. [10]. In the case of $B \parallel [111]$, this evolution follows the equations

$$E_\uparrow(E_i, n, B) = E_i + \frac{1}{2}(a_n + b_n) + \frac{1}{2}\left[(a_n - b_n)^2 + 4\hbar\frac{eB}{m_e}\left(\frac{2P_\perp^2}{m_e}\right)(n+1)\right]^{1/2}, \quad (5)$$

$$E_\downarrow(E_i, n, B) = E_i + \frac{1}{2}(c_{n-1} + d_{n-1}) + \frac{1}{2}\left[(c_{n-1} - d_{n-1})^2 + 4\hbar\frac{eB}{m_e}\left(\frac{2P_\perp^2}{m_e}\right)n\right]^{1/2}, \quad (6)$$

where E_i is the confinement energy already calculated and shown in Fig. 2, $n = 0, 1, 2, \ldots$ is the orbital number, $\uparrow$ and $\downarrow$ stand for spin-up and spin-down states, respectively, and the terms a_n, b_n, c_n, and d_n are given by

$$a_n = \hbar\omega_t^-\left(n + \frac{1}{2}\right) + \frac{1}{2}g_l^-\mu_B B, \quad (7)$$

$$b_n = \hbar\omega_t^+\left(n + \frac{3}{2}\right) - \frac{1}{2}g_l^+\mu_B B, \quad (8)$$

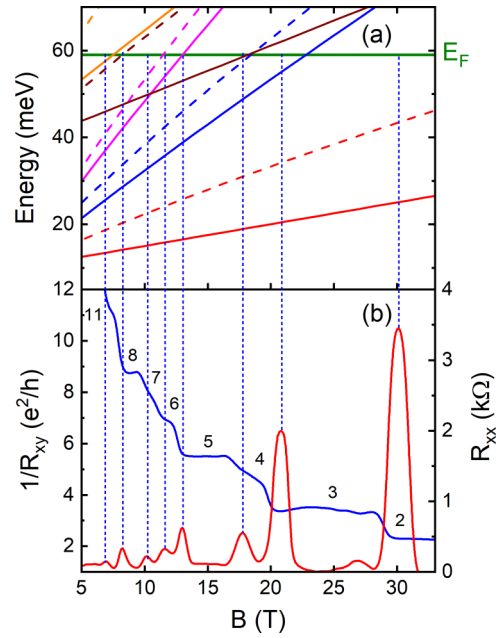

FIG. 3. (a) Fan chart of the spin-split Landau levels vs magnetic field for the first (E_{L1}) and second longitudinal (E_{L2}) and first oblique (E_{O1}) subbands. The colors correspond to orbital numbers $n = 0$ to $n = 2$ for E_{L1}, $n = 0$ for E_{L2}, and $n = 0$ for E_{O1}, and solid (dashed) lines represent spin-down (spin-up) states. The green solid line is the calculated Fermi energy position. (b) Longitudinal (R_{xx}) and the inverse of transverse ($1/R_{xy}$) resistance component vs B. The filling factors are indicated on the $(1/R_{xy})\times B$ curve for comparison to the predicted values shown in (a) and in Fig. 1(b).

$$c_n = \hbar\omega_t^-\left(n + \frac{3}{2}\right) - \frac{1}{2}g_l^-\mu_B B, \quad (9)$$

$$d_n = \hbar\omega_t^+\left(n + \frac{1}{2}\right) + \frac{1}{2}g_l^+\mu_B B. \quad (10)$$

In this Mitchell and Wallis approach, the energy of Landau levels depends on the far-band contributions to the transverse masses $m_t^\pm$ and longitudinal g factors $g_l^\pm$ in the valence (+) and conduction (−) bands. The transverse cyclotron frequency is $\omega_t^\pm = eB/m_t^\pm$ and μ_B is the Bohr magneton. The term $2P_\perp^2/m_e$ comes from the perpendicular interband momentum matrix element already mentioned above.

Figure 3(a) presents the fan chart of the spin-split Landau levels versus the magnetic field B for the first and second longitudinal ($E_{L1} = 10$ meV and $E_{L2} = 38$ meV) and first oblique subband ($E_{O1} = 42$ meV) subbands. The solid (dashed) lines represent the calculated energy values for spin-down (spin-up) states and the colors are related to the Landau levels from $n = 0$ to $n = 2$ for the first longitudinal, $n = 0$ for the second longitudinal, and $n = 0$ for the first oblique subbands. From this diagram, one can predict the sequence of filling factors present in the quantum Hall effect. For example, in the magnetic field interval from 13 to 17 T, five longitudinal sublevels are below the Fermi energy, resulting in a filling factor of $\nu = 5$, as the longitudinal valley is nondegenerate. Now, in the region between 7 and 8.2 T, eight longitudinal and one oblique sublevels are contributing to the transport ($E < E_F$),

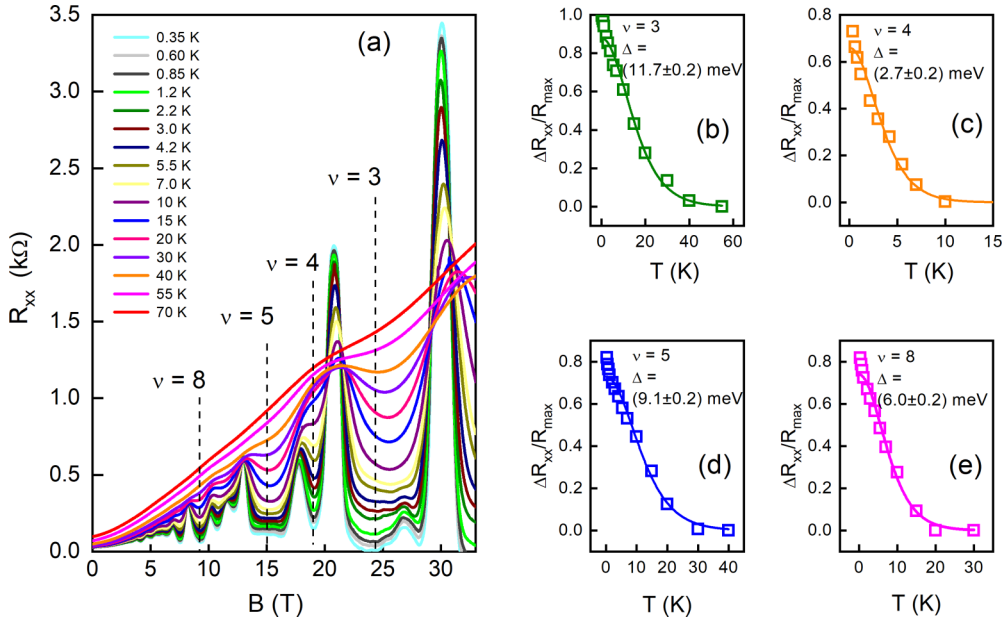

FIG. 4. (a) Plot of R_{xx} vs B measured at temperatures from 0.35 to 70 K. Some specific filling factors are indicated. (b)–(e) Graphs of $\Delta R_{xx}/R_{\max}$ vs T for each filling factor represented by square symbols together with the best fits (solid lines) using the thermal term of Lifshitz-Kosevich equation. The values of Δ obtained from the best fits are labeled inside the graphs.

which yields a filling factor $\nu = 11$, as the oblique level is $3\times$ degenerate. Due to the low magnetic field in this region (low resolution in the spin splitting), the plateau for $\nu = 11$ is not well defined, but the contribution of the first oblique level with spin-up state (solid orange line) is evidenced by the jump of 3 in the filling factor sequence (from 8 to 11). Hence, the fan chart predicts the filling factors of $\nu = 11$, 8, 7, 6, 5, 4, 3, and 2 in agreement with the filling factors sequence presented in Figs. 1(b) and 3(b). For the fan chart calculation in Fig. 3(a), the values of $m_t^+ = -0.102m_e$, $g_l^+ = -2.61$ and $g_l^- = 1.72$ were kept fixed [17], while the values of m_t^- and $2P_\perp^2/m_e$ were used as free parameters. The following best values were found in the calculations: $m_t^- = 0.105$, 0.048, and $0.025m_e$ and $\frac{2P_\perp^2}{m_e} = 1.2$, 2.5, and 4.0 eV for the first longitudinal, second longitudinal, and first oblique subbands, respectively. It is important to notice that these free parameter values differ from the ones published for bulk PbTe [17] but they are still acceptable as they provide a reliable nonparabolicity and a consequent nonlinearity in the magnetic field evolution of the Landau levels [10].

D. Temperature dependence

We investigate the temperature dependence of the longitudinal magnetoresistance R_{xx} to obtain a picture of the energy separation between two adjacent Landau levels and the mobility gaps in the QW sample. In Fig. 4(a), we plot the R_{xx} curves for temperatures from 0.35 to 70 K as a function of B with the indicated filling factors of $\nu = 8$, 5, 4, and 3. We can use the thermal damping term of the Lifshitz-Kosevich (LK) equation, $\Delta R_{xx}/R_{\max} = x/\sinh(x)$ with $x = 2\pi^2 k_B T/\Delta$, to extract the energy separation Δ between the LL centers. For each filling factor, we identify a maximum $R_{\max}$ (taken from the next nearest peak at the low-field side) and a minimum $R_{\min}$ resistance values in the R_{xx} curve and the resistance difference $\Delta R_{xx} = R_{\max} - R_{\min}$ is obtained by subtracting them. The values of $\Delta R_{xx}/R_{\max}$ as a function of temperature for the respective filling factor are presented in Figs. 4(b)–4(e) together with the best fits using the thermal LK expression, from which the Δ value is obtained. If we calculate the LL separation energies directly from the expression $E_{\rm LL} = \hbar\omega_c$, where $\omega_c = eB/m_t^+$, the obtained values are 10, 17, 22, and 27 meV for $B = 9.2$, 15, 19, and 24 T, respectively. These values are higher than the ones obtained for Δ from the LK fittings. This is a consequence of the large g factor of PbTe that leads to larger values of Zeeman spin-splitting gaps as compared to the energy separation of two adjacent Landau levels.

The activation energy (E_a) for each filling factor can be obtained if we consider thermally activated transport $R_{\min} = R_0 e^{-E_a/2k_BT}$, where R_0 is the zero-field resistance. In Fig. 5(a)

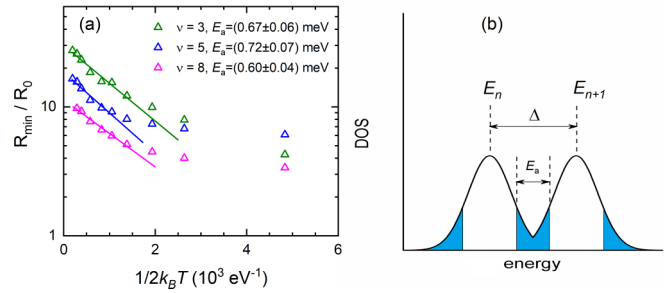

FIG. 5. (a) Plot of $R_{\min}/R_0$ as a function of the inverse of $2k_BT$ and the linear fittings (solid lines) to the data. The values of activation energy E_a obtained from the fits for each filling factor are displayed in the graph. (b) A pictorial description of the energies and density of states. The LK energy gap Δ corresponds to the energy separation between the LL centers. The activation energy E_a relative to the mobility gap delimits the region of the localized state (filled areas in blue).

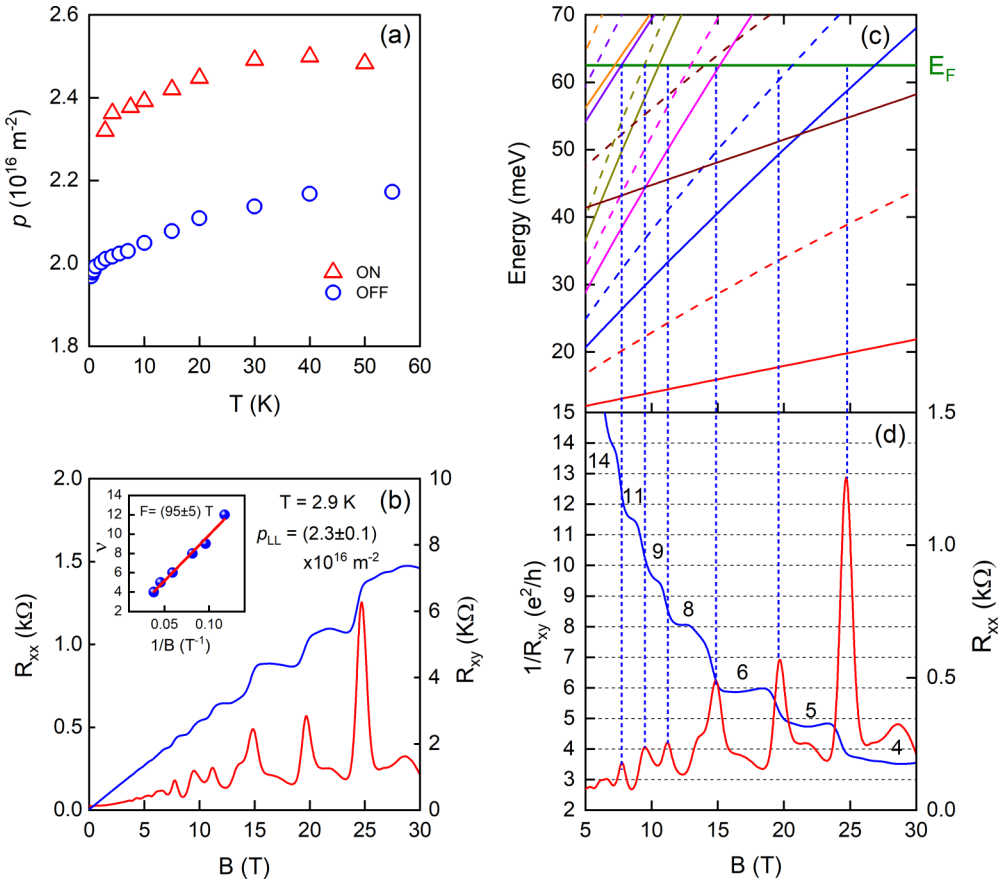

FIG. 6. (a) Carrier density obtained from Hall effect measurements at temperatures from 0.35 to 60 K with light switched on ($p_{\rm Hall}^{\rm ON}$, red triangles) and off ($p_{\rm Hall}^{\rm OFF}$, blue circles). (b) R_{xx} and R_{xy} resistance components measured under illumination at $T = 2.9$ K. The inset plots the filling factors ν as assigned in (d) vs the inverse magnetic position of the R_{xx} minima. The oscillations frequency F and the carrier density $p_{\rm LL}^{\rm ON}$ in the quantum well are obtained from the linear fit (red line). (c) Fan chart of the spin-split Landau levels for the first (E_{L1}) and second longitudinal (E_{L2}) and first oblique (E_{O1}) subbands. The colors correspond to orbital numbers $n = 0$ to $n = 3$ for E_{L1}, $n = 0$ and $n = 1$ for E_{L2}, and $n = 0$ for E_{O1}, and solid (dashed) lines represent spin-down (spin-up) states. The green solid line is the calculated Fermi energy position under illumination. (d) A plot of $1/R_{xy}$ in units of (e^2/h) vs B with the filling factors $\nu = 14$, 11, 9, 8, 6, 5, and 4 assigned to the plateaus.

we plot the logarithm of $R_{\rm min}/R_0$ as a function of the inverse of $2k_BT$ and, hence, the values of E_a are obtained from the slopes of the fittings (solid lines). These activation energies that correspond to the mobility gaps are in the order of 1 meV, much smaller than the energies found for the separation between LLs. This result indicates that the region of localized states is mainly placed in the tails of the density of states (DOS) curve, as illustrated in Fig. 5(b).

E. Effect of illumination

We also investigated the *p*-type PbTe QW sample illuminated with a commercial red LED. Figure 6(a) shows the carrier concentration obtained from Hall effect measurements, in the temperature range 0.35–60 K, performed under illumination ($p_{\rm ON}$, red triangles) and dark conditions ($p_{\rm OFF}$, blue circles). We find that the total Hall carrier density at 2.9 K increases from $p_{\rm Hall}^{\rm OFF} = (2.01 \pm 0.01)\times 10^{16}$ m^{-2} to $p_{\rm Hall}^{\rm ON} = (2.32 \pm 0.01)\times 10^{16}$ m^{-2}. Using this value of $p_{\rm Hall}^{\rm ON}$, the calculated Fermi energy under illumination is found to be (62.5 ± 1) meV, 3.5 meV higher than the value at dark conditions. For this Fermi energy, we still have the same two longitudinal and one oblique subbands occupied [see Fig. 2(b)] as in the dark situation. Nevertheless, the clear change in the R_{xx} and R_{xy} traces under illumination plotted in Fig. 6(b) in comparison to the dark situation [Fig. 1(a)] indicates a modification in the Landau level occupation due to the increase in the carrier concentration. Figure 6(d) plots the inverse of transverse resistance $1/R_{xy}$ under illumination, in units of (e^2/h), as a function of B (blue curve), from where the filling factors sequence $\nu = 14$, 11, 9, 8, 6, 5, and 4 can be inferred. The filling factor $\nu = 7$ is also not well defined like in the dark case. The plot of ν vs $1/B$, shown in the inset of Fig. 6(b), also exhibits a linear behavior and the oscillations frequency $F = (95 \pm 5)$ T obtained from the linear fit gives a 2D hole density $p_{\rm LL}^{\rm ON} = (2.3 \pm 0.1)\times 10^{16}$ m^{-2} in the quantum well. Although this carrier concentration is identical within the experimental error to the Hall value, the nonzero values in the R_{xx} trace in the integer quantum Hall regime [see Figs. 6(b) and 6(d)] suggest that a parallel conduction takes place when light is switched on.

Following the same procedure as for the dark case, we use Eqs. (5)–(10) to predict the sequence of filling factors when the sample is illuminated. Figure 6(c) presents the fan chart

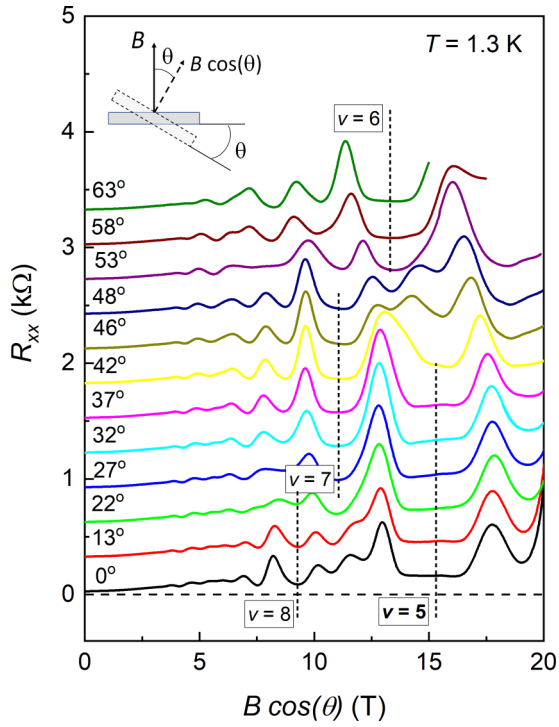

FIG. 7. Angle dependence of the R_{xx} as a function of the applied magnetic field (the curves are offset for clarity). The sample is rotated *in situ* while the magnetic field is kept in a fixed direction as shown in the inset. The sequence of filling factors strongly changes upon tilting the sample.

of the spin-split Landau levels, in which the solid (dashed) lines represent the calculated energy values for spin-down (spin-up) states and the colors are related to the Landau levels from $n = 0$ to $n = 3$ for the first longitudinal (E_{L1}), $n = 0$ and $n = 1$ for the second longitudinal (E_{L2}), and $n = 0$ for the first oblique (E_{O1}) subbands. For this calculation, the same fixed values for m_t^+, g_l^+, and g_l^- were used, while the following best values were found during the simulation: $m_t^- = 0.130$, 0.080, and $0.02m_e$ and $\frac{2P_\perp^2}{m_e} = 1.5$, 2.0, and 3.0 eV for the first longitudinal, second longitudinal, and first oblique subbands, respectively. These free parameter values are close to the ones found for the dark case. The calculated fan chart of Fig. 6(c) also predicts well the sequence of filling factors for the PbTe QW under illumination. For instance, at the plateau region assigned as $\nu = 6$, six longitudinal sublevels are below the Fermi energy. Now, for the plateau labeled as $\nu = 14$, 11 longitudinal and 1 oblique sublevels are occupied, and a jump from 11 to 14 occurs as the spin-down oblique level starts to contribute. As expected for a QW with higher carrier density, a sequence of filling factors with higher values is observed as the sample is illuminated.

F. Angular dependence

We present here the angle-dependent measurements of R_{xx} that were carried out to investigate the interplay between multiple valleys before illumination. Figure 7 exhibits the angle dependence of the R_{xx} as a function of the applied magnetic field. The sample is rotated *in situ* while the magnetic field is kept in a fixed direction. The field component perpendicular to the sample surface makes an angle θ with the fixed direction (see inset). This graph shows that the sequence of filling factors is strongly altered upon changing the tilt angle θ. While some filling factors are suppressed with increasing tilt angles, for instance $\nu = 5$ and 8 indicated by the dashed lines in Fig. 7, other filling factors appear in certain regions, see $\nu = 7$ for $\theta > 22^\circ$ or $\nu = 6$ for $\theta > 50^\circ$. These changes can be qualitatively understood by recalling that the perpendicular component of the magnetic field scales with $B\cos(\theta)$ while the Zeeman remains constant. Also, the multivalley character of PbTe makes a quantitative analysis very complex, which is beyond the scope of this work.

IV. CONCLUSIONS

The investigation of Shubnikov–de Haas oscillations and integer quantum Hall effect in a 10 nm-thick p-type PbTe quantum well was presented here. The results revealed that the transport occurs through the two-dimensional hole gas confined in the quantum well with negligible parallel conduction at low temperatures. We derived the subband energy diagram and found that two longitudinal and one oblique subbands are occupied and contribute to electrical transport. From the magnetic field evolution of the Landau levels and considering the Zeeman spin splitting of the subbands, we were able to explain the filling factors sequence observed in the R_{xy} component of magnetoresistance. Due to the increase in the total carrier density of the QW system during illumination, a different plateau sequence in the integer quantum Hall effect with higher filling factors was found in comparison to the dark situation. Due to the high Landé g factor of PbTe that leads to large Zeeman spin splittings, the energy gap obtained from the fittings to the thermal damping term of the Lifshitz-Kosevich equation was determined to be smaller than the cyclotronic energy separation between two adjacent Landau levels. The angular dependence analysis showed that the sequence of filling factors is strongly modified upon tilting the sample, as expected for a semiconductor material with multiple valleys.

ACKNOWLEDGMENTS

We thank the Brazilian Funding Agencies CAPES and CNPq (Grant No. 305764/2018-7) for financial support. This work was also supported by HFML-RU/NWO-I, a member of the European Magnetic Field Laboratory (EMFL).

[1] H. Zogg, Photovoltaic IV-VI on silicon infrared devices for thermal imaging applications, Proceedings of SPIE **3629**, 52 (1999).

[2] Z. Han, V. Singh, D. Kita, C. Monmeyran, P. Becla, P. Su, J. Li, X. Huang, L. C. Kimerling, J. Hu, K. Richardson, D. T. H. Tan, and A. Agarwal, On-chip chalcogenide glass waveguide-integrated mid-infrared PbTe detectors, Appl. Phys. Lett. **109**, 071111 (2016).

[3] G. Springholz, T. Schwarzl, M. Aigle, H. Pascher, and W. Heiss, 4.8 μm vertical emitting PbTe quantum-well lasers based on

high-finesse EuTe/$Pb_{1-x}Eu_x$Te microcavities, Appl. Phys. Lett. **76**, 1807 (2000).

[4] A. Majumdar, H. Z. Xu, S. Khosravani, F. Zhao, L. Jayasinghe, and Z. Shi, High power light emission of IV–VI lead salt multiple-quantum-well structure grown by molecular-beam epitaxy on ⟨111⟩ BaF_2 substrate, Appl. Phys. Lett. **82**, 493 (2003).

[5] A. Khiar, M. Eibelhuber, V. Volobuev, M. Witzan, A. Hochreiner, H. Groiss, and G. Springholz, Vertical external cavity surface emitting PbTe/CdTe quantum dot lasers for the mid-infrared spectral region, Opt. Lett. **39**, 6577 (2014).

[6] G. Grabecki, Quantum ballistic phenomena in nanostructures of paraelectric PbTe, J. Appl. Phys. **101**, 081722 (2007).

[7] M. L. Peres, H. S. Monteiro, V. A. Chitta, S. de Castro, U. A. Mengui, P. H. O. Rappl, N. F. Oliveira, Jr., E. Abramof, and D. K. Maude, Experimental investigation of spin-orbit coupling in n -type PbTe quantum wells, J. Appl. Phys. **115**, 093704 (2014).

[8] S. Jin, H. Wu, and T. Xu, Large Rashba splitting in highly asymmetric CdTe/PbTe/PbSrTe quantum well structures, Appl. Phys. Lett. **95**, 132105 (2009).

[9] S. Murakami, N. Nagaosa, and S.-C. Zhang, Spin-Hall Insulator, Phys. Rev. Lett. **93**, 156804 (2004).

[10] V. A. Chitta, W. Desrat, D. K. Maude, B. A. Piot, N. F. Oliveira, Jr., P. H. O. Rappl, A. Y. Ueta, and E. Abramof, Multivalley transport and the integer quantum Hall effect in a PbTe quantum well, Phys. Rev. B **72**, 195326 (2005).

[11] F. S. Pena, M. L. Peres, M. J. P. Pirralho, D. A. W. Soares, C. I. Fornari, P. H. O. Rappl, and E. Abramof, Fast photoresponse and high parallel transport in n-type PbTe/PbEuTe quantum wells, Appl. Phys. Lett. **111**, 192105 (2017).

[12] E. A. de Andrada e Silva, Optical transition energies for lead-salt semiconductor quantum wells, Phys. Rev. B **60**, 8859 (1999).

[13] J. O. Dimmock and G. B. Wright, Band Edge Structure of PbS, PbSe, and PbTe, Phys. Rev. **135**, A821 (1964).

[14] E. Abramof, E. A. de Andrada e Silva, S. O. Ferreira, P. Motisuke, P. H. O. Rappl, and A. Y. Ueta, Optical spectra of PbTe/Pb_{1-x}EuxTe quantum wells, Phys. Rev. B **63**, 085304 (2001).

[15] D. L. Mitchell and R. F. Wallis, Theoretical energy-band parameters for the lead salts, Phys. Rev. **151**, 581 (1966).

[16] H. Burkhard, G. Bauer, and W. Zawadzki, Band-population effects and intraband magneto-optical properties of a many-valley semiconductor: PbTe, Phys. Rev. B **19**, 5149 (1979).

[17] G. Bauer, H. Pascher, and W. Zawadzki, Magneto-optical properties of semimagnetic lead chalcogenides, Semicond. Sci. Technol. **7**, 703 (1992).